AGU PUBLICATIONS

JGR

Journal of Geophysical Research: Space Physics

RESEARCH ARTICLE

10.1002/2015JA021168

Key Points:
- New ISR mode at Jicamarca measures topside parameters
- ISR data compared with C/NOFS CINDI measurements, SAMI2-PE model
- Extreme, rapid temperature variations in topside poorly understood

Correspondence to:
D. L. Hysell,
dlh37@cornell.edu

Citation:
Hysell, D. L., M. A. Milla, F. S. Rodrigues, R. H. Varney, and J. D. Huba (2015), Topside equatorial ionospheric density, temperature, and composition under equinox, low solar flux conditions, *J. Geophys. Res. Space Physics*, *120*, 3899–3912, doi:10.1002/2015JA021168.

Received 26 FEB 2015
Accepted 15 APR 2015
Accepted article online 23 APR 2015
Published online 12 MAY 2015

Topside equatorial ionospheric density, temperature, and composition under equinox, low solar flux conditions

D. L. Hysell[1], M. A. Milla[2], F. S. Rodrigues[3], R. H. Varney[4], and J. D. Huba[5]

[1]Earth and Atmospheric Sciences, Cornell University, Ithaca, New York, USA, [2]Jicamarca Radio Observatory, Lima, Peru, [3]William B. Hanson Center for Space Sciences, University of Texas at Dallas, Richardson, Texas, USA, [4]SRI International, Menlo Park, California, USA, [5]Naval Research Laboratory, Washington, District of Colombia, USA

Abstract We present observations of the topside ionosphere made at the Jicamarca Radio Observatory in March and September 2013, made using a full-profile analysis approach. Recent updates to the methodology employed at Jicamarca are also described. Measurements of plasma number density, electron and ion temperatures, and hydrogen and helium ion fractions up to 1500 km altitude are presented for 3 days in March and September. The main features of the observations include a sawtooth-like diurnal variation in h_t, the transition height where the O^+ ion fraction falls to 50%, the appearance of weak He^+ layers just below h_t, and a dramatic increase in plasma temperature at dawn followed by a sharp temperature depression around local noon. These features are consistent from day to day and between March and September. Coupled Ion Neutral Dynamics Investigation data from the Communication Navigation Outage Forecast System satellite are used to help validate the March Jicamarca data. The SAMI2-PE model was able to recover many of the features of the topside observations, including the morphology of the plasma density profiles and the light-ion composition. The model, forced using convection speeds and meridional thermospheric winds based on climatological averages, did not reproduce the extreme temperature changes in the topside between sunrise and noon. Some possible causes of the discrepancies are discussed.

1. Introduction

This is an examination of the topside equatorial ionosphere made possible by some recent improvements in hardware and software at the Jicamarca Radio Observatory. We follow *Banks et al.* [1976] by defining the protonosphere as that region above 2000–3000 km altitude where H^+ is the dominant thermal ion and all reaction processes can be neglected. The topside ionosphere is then that part of the ionosphere above the F_2 peak and below the protonobase, where multiple ion species exist and where chemistry competes with transport in determining composition. Heat transport meanwhile dominates local heating and cooling in the topside and includes both thermal conductivity and energetic electron transport. (Below the *F* peak, chemical production and loss and heating and cooling essentially balance locally.) At low latitudes, the topside ionosphere is confined to the inner plasmasphere, whereas at middle and high latitudes, it resides in the outer plasmasphere and outside the plasmasphere, respectively.

The properties of the equatorial topside ionosphere are strongly influenced by the geomagnetic field which inhibits vertical transport locally. Since the magnetic field does not appear in the Hamiltonian of the plasma, it cannot affect the equilibrium configuration of the ionosphere. It can, however, retard the approach to equilibrium and effectively prevent it from being reached. Stark differences between the topside at equatorial and middle latitudes is evidence of the effect.

Topside light-ion composition at middle latitudes was studied by *González and Sulzer* [1996] during equinox, solar minimum conditions. They found that oxygen, hydrogen, and helium ions behave in accordance with 1-D diffusive equilibrium (i.e., hydrostatic balance mediated by the parallel ambipolar electric field). Oxygen and hydrogen ions undergo resonant charge exchange, with the former (latter) serving as a source for the latter (former) during the day (at night). The O^+/H^+ transition height (h_t, the altitude where the O^+ fraction falls below 50%) exhibited a diurnal variation between about 500 km and 1200–1400 km. The He^+ ion fraction maximized near h_t at 10–20%. (Under high solar flux conditions, He^+ abundances increase dramatically at middle latitudes, and He^+ can become the dominant species near h_t [*González et al.*, 2004; *West*, 2009]). Under conditions of extremely low solar flux, h_t decreases further [*Heelis et al.*, 2009; *Aponte et al.*, 2013].

©2015. American Geophysical Union. All Rights Reserved.

Heelis et al. [1990] studied He^+ abundances during solar minimum at middle and low latitudes on the basis of data from the DE 2 satellite. They identified a deep minimum in He^+ at the magnetic equator, where He^+ is always a minor species. They attributed this to $E \times B$ drifts at the equator which plunge the ionosphere to low altitudes each day, removing He^+ through recombination and preventing the accumulation of the species over multiday intervals. A controlling role for electric fields (and, by extension, thermospheric winds) at the equator was therefore implied. *González et al.* [1992] examined AE-E satellite data during solar minimum and found the equatorial h_t to vary between 750–825 km during the day and 550–600 km at night. He^+ was highly variable, always a minor species and exhibited peak daytime densities of about 10^3 cm^{-3} near 500 km altitude.

A number of studies have concentrated on the role of interhemispheric (meridional) winds and the adiabatic heating and cooling of the topside ionosphere at low latitudes, particularly near the solstices [*Rishbeth et al.*, 1977; *Bailey and Heelis*, 2000; *Venkatraman and Heelis*, 1999, 2000]. These studies identified a topside temperature trough near the dip equator. *Balan et al.* [1997] associated the nighttime trough not with meridional winds but with the adiabatic expansion of the plasma driven by the prereversal enhancement of $E \times B$ convection. *Bailey* [1983] also studied the effect of $E \times B$ convection and found that there were significant effects on plasma density and temperature during the day but not at night. *Bailey et al.* [1993] were able to reproduce the morphology of the equatorial topside during the day in simulation but not at night unless the neutral winds were assumed to be small (zero).

In addition to heating by expansion and contraction, *Varney et al.* [2011] considered the relative effects of local heating and cooling, transverse and parallel advection, thermal conduction, and photoelectrons in establishing equilibrium topside ionospheric temperatures at the magnetic equator. Thermal conduction (down magnetic field lines) and energetic electron transport (up) were found to be the main heating agents in the topside, working together to balance local cooling. The energetic electron transport treatment was oversimplified, and so *Varney et al.* [2013] reexamined the problem, this time incorporating an energetic electron transport code in their numerical analysis (see below). In both studies, small variations in the density and height of the *F* layer were found to be able to shift the heat balance appreciably by regulating the penetration of energetic electrons into the topside, implying significant sensitivity of the topside thermal structure to electric fields and thermospheric winds and the development of the *F* region at off-equatorial latitudes.

A limited number of incoherent scatter data were available for the aforementioned studies, and those data suffered from certain systemic deficiencies which have since been corrected. In this paper, we undertake a more exhaustive study of the topside over Jicamarca during equinox conditions in 2013 when the $F_{10.7}$ solar flux index was low but not exceptionally so (95–125). After describing the manner of data acquisition and analysis, which has undergone improvement in recent years, representative data are presented. These are compared with a numerical model (SAMI2-PE), and the overall data/model agreement is assessed.

2. Experimental Method

Jicamarca topside data are analyzed using a "full-profile" approach like the one outlined by *Holt et al.* [1992] only with a few adaptations. This is in contrast to the "gated" analyses more routinely applied to incoherent scatter data. The motivations for using full-profile analysis with Jicamarca topside data were given by *Hysell et al.* [2008] and *Hysell et al.* [2009]. Our analysis yields estimates of topside electron and ion temperatures and light ion composition in addition to plasma density. A few special complications enter in the analysis of data from Jicamarca as described below.

The incoherent scatter experiment used for topside research at Jicamarca interleaves the traditional double-pulse Faraday rotation experiment developed by *Farley* [1969b] and *Pingree* [1990] with a long-pulse experiment. The long pulse is typically 1.6 ms long, and the combined experiment incorporates the transmission of one long pulse and two double-pulse pairs every 40 ms. Samples are acquired at a rate which is a multiple of 10 kHz, but digital boxcar averaging during data processing reduces the sample interval to 100 μs. The long-pulse data provide most of the information about the topside. The double-pulse data are useful for estimating ionospheric state parameters in the bottomside and near the *F* peak. Faraday rotation information from the double-pulse mode also provide a means of absolute density calibration [*Farley*, 1969a].

©2015. American Geophysical Union. All Rights Reserved.

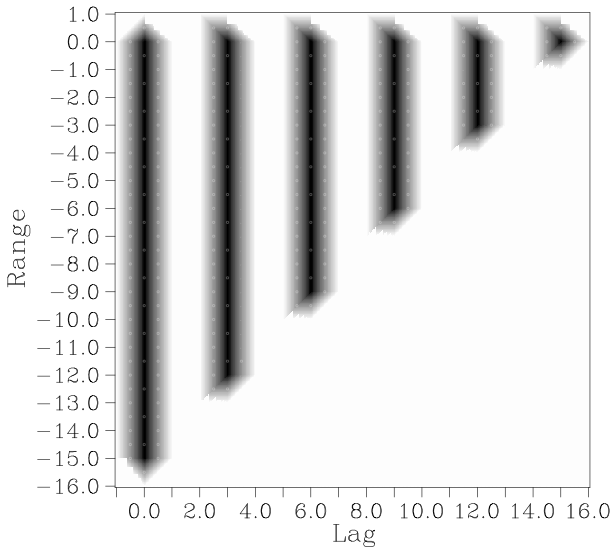

Figure 1. Six representative (of 16 possible) ambiguity functions for the long-pulse experiment. Plotter symbols indicate sample points for numerical quadrature (see text). For our experiments, lags are separated by τ = 100 μs and ranges by $c\tau/2$ = 15 km intervals.

The full-profile analysis is a global optimization in which the ionospheric state parameter profiles (plasma number density, electron and ion temperature, and light ion fractions) are found which minimize the discrepancy between predicted and measured data along with certain other cost or regularization parameters. The data are the measured lag product estimates along with their experimental variances, which arise from the stochastic nature of the radar data and the use of finite time averages as proxies for ensemble averages. While estimates of the full error covariances could well be used in the analysis, only the variances are used in our analysis at the present time. The analysis is carried out using the formulas in *Hysell et al.* [2008], who also describes how error analysis is performed. While neglecting the off-diagonal part of the error covariance matrix introduces inaccuracy in the overall error analysis, it should not bias the results significantly [*Huuskonen and Lehtinen*, 1996]. The error norm that is minimized is the usual chi-square parameter.

State parameter profiles are specified at certain discrete altitudes and then computed as continuous functions of altitude, as necessary, using interpolation. In our algorithm, cubic B-spline interpolation is used [see, e.g., *De-Boor*, 1978]. Each state variable is specified at typically 25 equally spaced (cardinal) knots.

Predictions of the lag products are computed from the state parameter profiles using standard incoherent scatter theory for magnetized ionospheric plasmas at small magnetic aspect angles, including the effects of Coulomb collisions [see *Sulzer and Gonzalez*, 1999; *Woodman*, 2004; *Milla and Kudeki*, 2006]. Incoherent scatter theory can be used to predict the radar scattering cross section and autocorrelation function at a given altitude for a given lag time. Combining these into lag product predictions necessitates the specification of the range-lag ambiguity functions, the instrument functions of the incoherent scatter radar [see, for example, *Lehtinen*, 1986; *Lehtinen and Huuskonen*, 1996; *Nygrén*, 1996]. (General treatments of the complete radar instrument function can be found in reviews by *Woodman* [1991] and *Lehtinen and Huuskonen* [1996]).

Figure 1 represents graphically six of the 16 lag products that define the long-pulse radar mode. The ambiguity functions are the averaging kernels that relate the scattering autocorrelation function, a continuous function of range and lag time, to the discrete lag products estimated in incoherent scatter radar (ISR) experiments. Gray scales in Figure 1 denote the weight. The shapes of the ambiguity functions depend on the transmitted pulse shape and the impulse response function of the receiver. Here the ambiguity functions are calculated just once at the start of data processing on the basis of measurements of the radar system and stored for later use in a table. Recent upgrades to the transmit and receive chains at Jicamarca have rendered the transmitted pulse and the receiver impulse response functions to be precisely box-car shaped for all intents and purposes.

The plotter symbols in Figure 1 give the positions of the discrete samples to be used in the theoretical prediction of the lag products, which requires numerical quadrature. Figure 2 illustrates our quadrature scheme in more detail. To the left are shown the weights for a uniform sample grid in two dimensions following Simpson's rule for numerical integration (which are just the product of the weights for one-dimensional numerical integration). We have found no appreciable change in the computational results when doubling the density of sample points in range and in lag compared to what is depicted in Figure 1. We have furthermore found no appreciable change in results when replacing the weights from Simpson's method with the sparse-grid approximation shown to the right of the figure.

©2015. American Geophysical Union. All Rights Reserved.

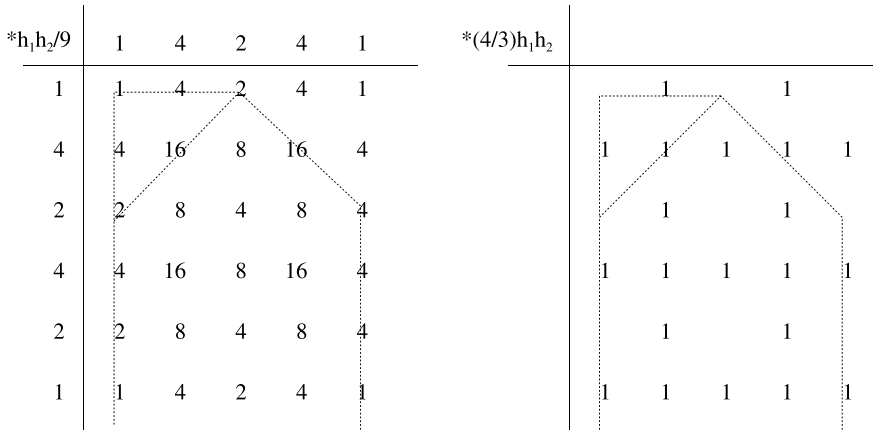

Figure 2. (left) Two-dimensional quadrature scheme based on Simpson's rule. (right) Simplified quadrature scheme using coarse, sparse sampling.

In practice, the autocorrelation functions are evaluated at every range and lag of interest, tabulated, and then used, together with the tabulated ambiguity function weights, to compute the predicted lag profiles. As the ambiguity functions for different lag products overlap, most autocorrelation function values are used multiple times.

The range-lag ambiguity functions describe two dimensions of a three-dimensional averaging kernel important for interpreting data from Jicamarca. The third dimension is that of magnetic aspect angle. Jicamarca illuminates a span of magnetic aspect angles approximately 1° wide, and the aspect-angle variation of the radar scattering cross section and autocorrelation function generally must be considered in the aforementioned numerical quadrature [e.g., *Milla and Kudeki*, 2011; *Kudeki and Milla*, 2011]. The relevant controlling function for volume scatter is the backscatter gain [*Bowles et al.*, 1962]. Calculations of the backscatter gain for Jicamarca show that the function, with its dependence on hour angle integrated away, is reasonably well approximated by a Gaussian function with a half width of $\sigma = 0.62°$. A quadrature scheme based on Gauss-Hermite integration is indicated. A three-point rule places samples at the midpoint of the beam and at the midpoint $\pm 1.225\sigma$ with corresponding weights of 1.18 and 0.295. While this consideration is very likely important for experiments conducted with Jicamarca's on-axis antenna position, it has not been found to be important at the 4.5° position used for the experiments described here.

The optimization algorithm is iterative and relies upon a good initial guess for success. The initial guess for the electron density profile is derived in part from the zero-lag profile. The transmitted pulse shape is deconvolved from this profile to yield an estimate of the power profile with good range resolution. Deconvolution is performed using Tikhonov regularization [see, e.g., *Menke*, 1984; *Tarantola*, 1987; *Aster et al.*, 2005]. Although the deconvolution problem is linear, we solve it iteratively, using a nonnegative least squares algorithm which only admits nonnegative solutions [*Lawson and Hanson*, 1987]. The power profile thus obtained is combined with the power profile from the double-pulse experiment, which is accurate at lower altitudes. Power is converted to electron density taking into account the effects of range and the influence of the electron-ion temperature ratio on the scattering cross section. Finally, the density profile is normalized to the profile obtained from Faraday rotation.

Initial guesses for the electron and ion temperature and the proton fraction are obtained using a grid search. Of the order of 1000 candidate profile sets are examined, a chi-square value calculated for each one. The profile set with the minimum chi-square becomes the initial guess. The candidate functions are derived from simple, parameterized functions inspired by profile shapes found using radar experiments based on coded pulses. The grid search typically yields an initial guess with a model prediction error (chi-square divided by the number of data) no more than about 2.

During iteration, the penalty function being minimized includes chi-square plus 10 regularization parameters. Regularization is necessary to reduce the solution space of the optimization problem, which is mixed determined and to improve stability and guarantee convergence. Five of the regularization parameters minimize the curvature of the five state parameter profiles. Five more parameters constrain the ion

©2015. American Geophysical Union. All Rights Reserved.

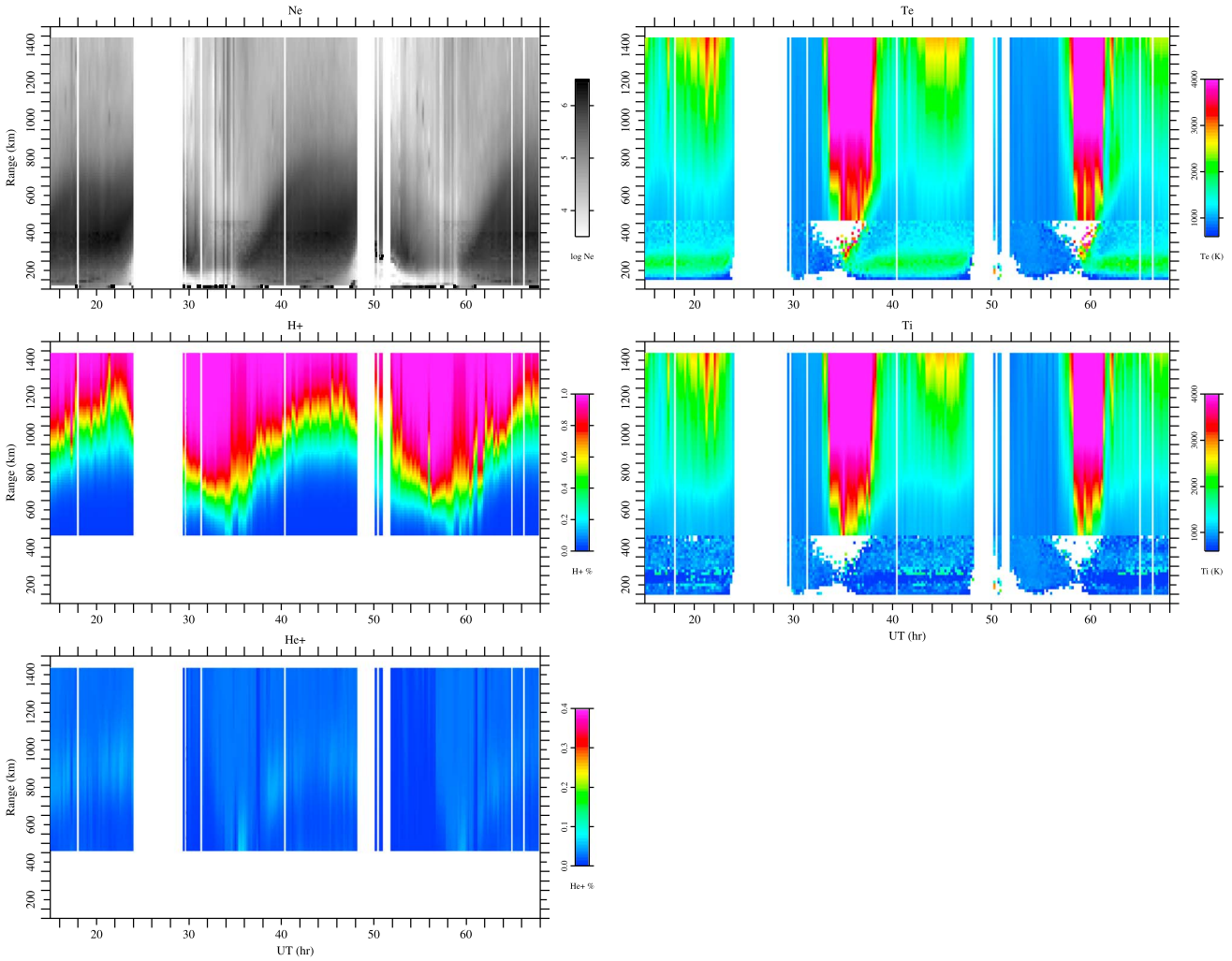

Figure 3. Incoherent scatter measurements for 11–13 March 2013. (left column) Electron density, H^+ ion fraction, and He^+ ion fraction. (right column) Electron temperature and ion temperature. UT = LT + 5 h. White space denotes missing data.

temperature at low altitudes, the proton fraction at high altitudes, the T_e/T_i ratio (which should not be less than 1), the oxygen ion fraction (which should be between 0 and 100%), and the He^+ abundance, which is only predicted to the extent there is support for it in the data.

Optimization is performed iteratively using a Levenberg Marquardt scheme [*Levenberg*, 1944; *Marquardt*, 1963]. Iteration to convergence generally produces fits to the data with a model prediction error close to 1, implying that the fitting has been neither overregularized nor under-regularized.

At present, we make no provisions for assigning different temperatures to different ion species. This is potentially an important effect, particularly around sunrise, and its neglect may be introducing a bias in helium ion concentration estimates [*Sulzer and González*, 1996]. The problem remains to be addressed in the future.

3. Experimental Results

Experiments were conducted in March and September 2013 with the results shown in Figures 3 and 4, respectively. We plot all of the data collected during the two 3 day campaigns. Data gaps arise from brief transmitter outages, echoes from debris and other clutter, and from coherent echoes associated with equatorial spread *F*, which is practically ubiquitous after sunset during equinox. The $F_{10.7}$ solar flux index was 125 (95) during the March (September) experiments.

©2015. American Geophysical Union. All Rights Reserved.

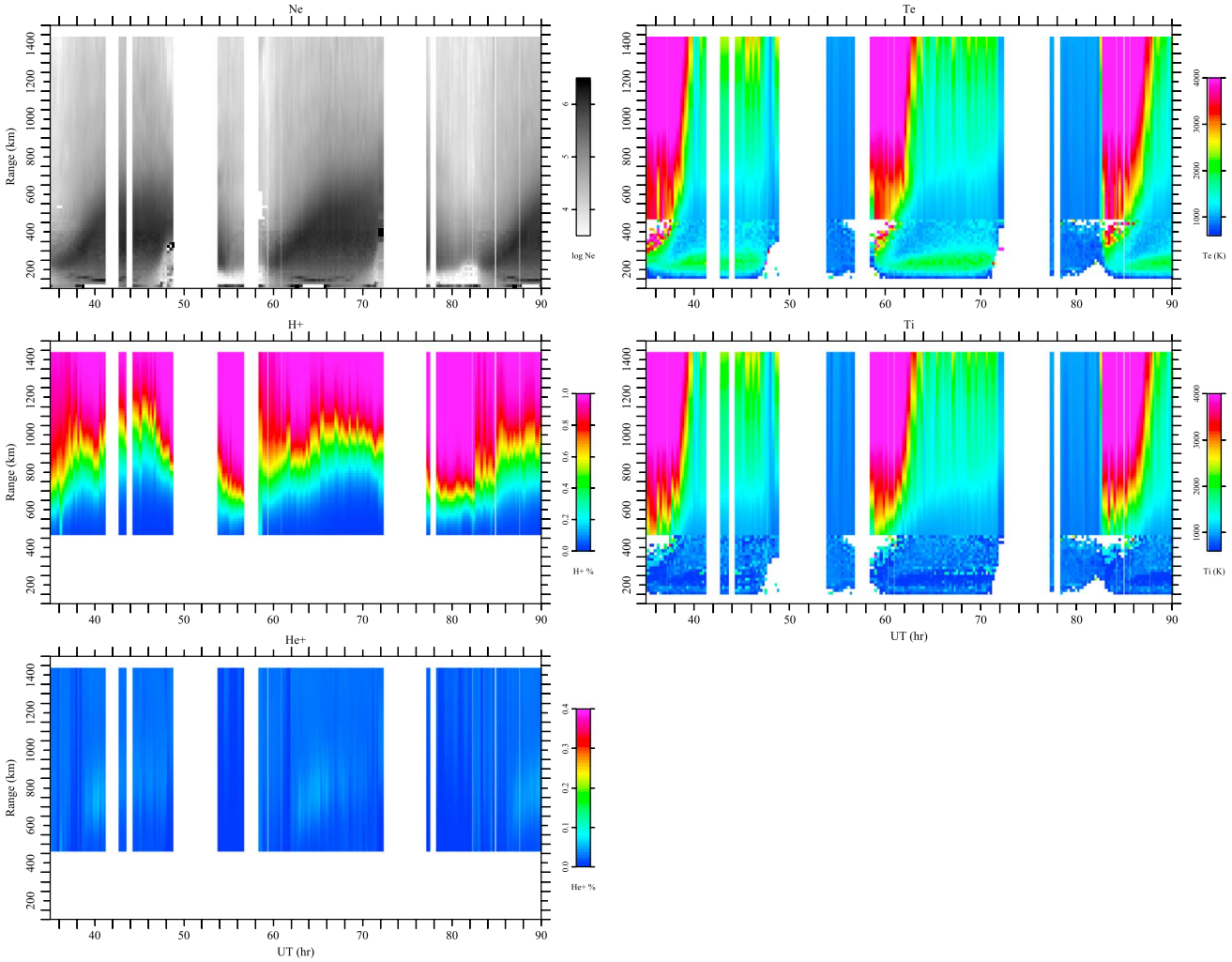

Figure 4. Same as Figure 3 except for 9–11 September 2013. UT = LT + 5 h.

The most important characteristics of the data are as follows:

1. The h_t follows a diurnal pattern with a sawtooth shape. The transition height varied between 600–1100 km in March and 600–1000 km in September.
2. A layer of He^+ resides just below h_t and is most evident in the morning. The He^+ fraction was always less than 10%, and the layer was stronger in March than September.
3. The electron temperature in the topside undergoes a strong maximum for a few hours after dawn, exhibits a local minimum around midday, and then exhibits a local maximum in late afternoon before assuming its nighttime minimum, when the temperatures are equal and uniform. Topside temperatures were somewhat higher in March than September.
4. The electron temperature greatly exceeds the ion temperature in the F_1 region throughout the day and near the F peak briefly at sunrise.

A limited validation of the Jicamarca analysis has been performed by comparing the results with measurements from the Coupled Ion Neutral Dynamics Investigation (CINDI) instrument on the Communication Navigation Outage Forecast System (C/NOFS) satellite during close conjunctions of the satellite orbit with the volume probed by Jicamarca occurring in March 2013. The CINDI instrument includes a retarded potential analyzer and ion drift meter [see, e.g., *Heelis and Hanson*, 1998]. The former provides estimates of plasma number density, composition, and ion temperature.

Figure 5 shows the results of comparing CINDI and Jicamarca data directly during conjunctions which occurred near sunrise. Overall, the agreement appears to be satisfactory over a broad range of topside

©2015. American Geophysical Union. All Rights Reserved.

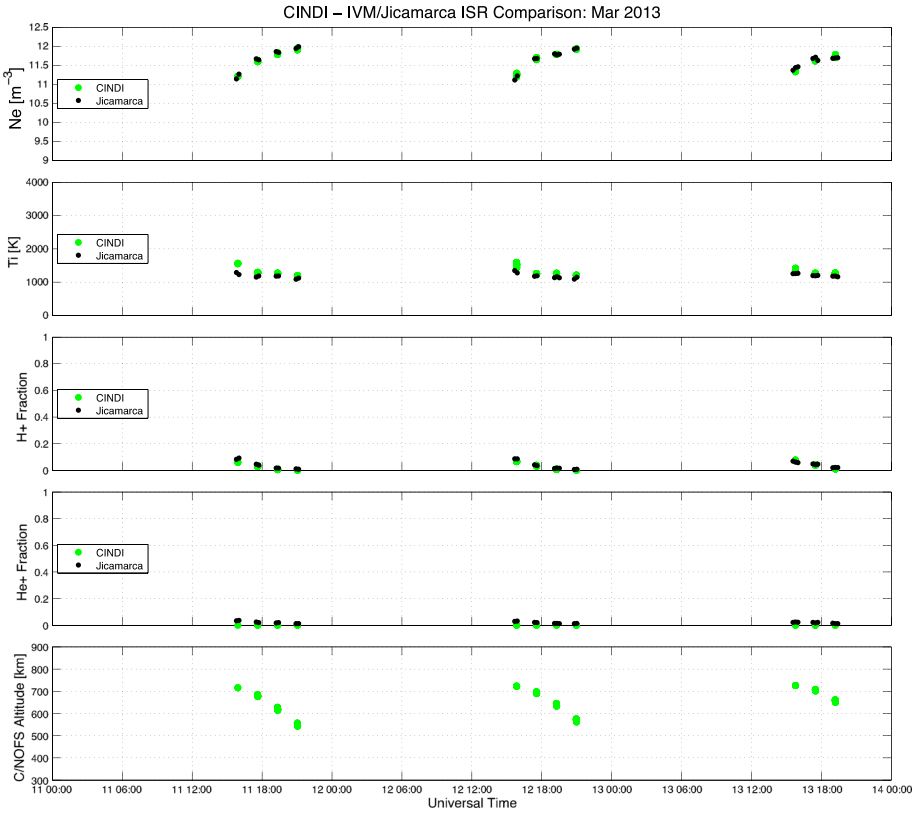

Figure 5. Comparison of Jicamarca and CINDI measurements during C/NOFS satellite conjunctions in March 2013. From top to bottom: (first row) Electron number density. (second row) Ion temperature. (third row) Hydrogen ion fraction. (fourth row) Helium ion fraction. (fifth row) C/NOFS satellite altitude during conjunctions. UT = LT + 5 h.

altitudes. There appears to be a tendency for Jicamarca to show lower ion temperatures than CINDI above about 700 km altitude, although the data are too few in number to support the idea of a trend. A more extensive database is presently being assembled for more complete validation.

4. Model and Analysis

For analysis, we use the SAMI2-PE ionospheric model which is based on SAMI2 (SAMI2 is Another Model of the Ionosphere) [*Huba et al.*, 2000]. SAMI2 incorporates neutral parameters and forcing from the NRLMSIS00 (Naval Research Laboratory Mass Spectrometer and Incoherent Scatter 2000) and HWM93 (Horizontal Wind Model 1993) empirical models and then solves self-consistently for plasma density, temperature, and composition in two dimensions in a nonorthogonal, corrected magnetic dipole coordinate system. Additional forcing is imported from the empirical $E \times B$ drift model of *Scherliess and Fejer* [1999].

SAMI2 models seven ion species plus electrons, taking into account 28 chemical reactions in addition to photo-production of O^+, He^+, N_2^+, and O_2^+. Nighttime photo-production sources are considered. The chemical reactions modeled by SAMI2 most critical for the topside include the photo-production of helium ions, charge exchange between oxygen and hydrogen, and helium-ion recombination via interaction with molecular oxygen and molecular nitrogen.

SAMI2 solves the conservation equations corresponding to the first five moments of the Boltzmann equation, assuming Maxwellian distribution functions, and with a heat flow vector prescribed by Fourier's law [see, e.g., *Schunk and Nagy*, 2004]. Ions in the model are heated by electrons, exchange heat between themselves, and are cooled by the neutrals locally, while heat is transported by conduction parallel to B, advection parallel to B, and convection perpendicular to B. Thermal electrons are heated by photoelectrons (see below) and cooled by neutrals and ions locally, while heat is transported by conduction parallel to B and convection perpendicular to B. Quasi-neutrality is mediated by the ambipolar electric field, but parallel currents are not considered explicitly.

©2015. American Geophysical Union. All Rights Reserved.

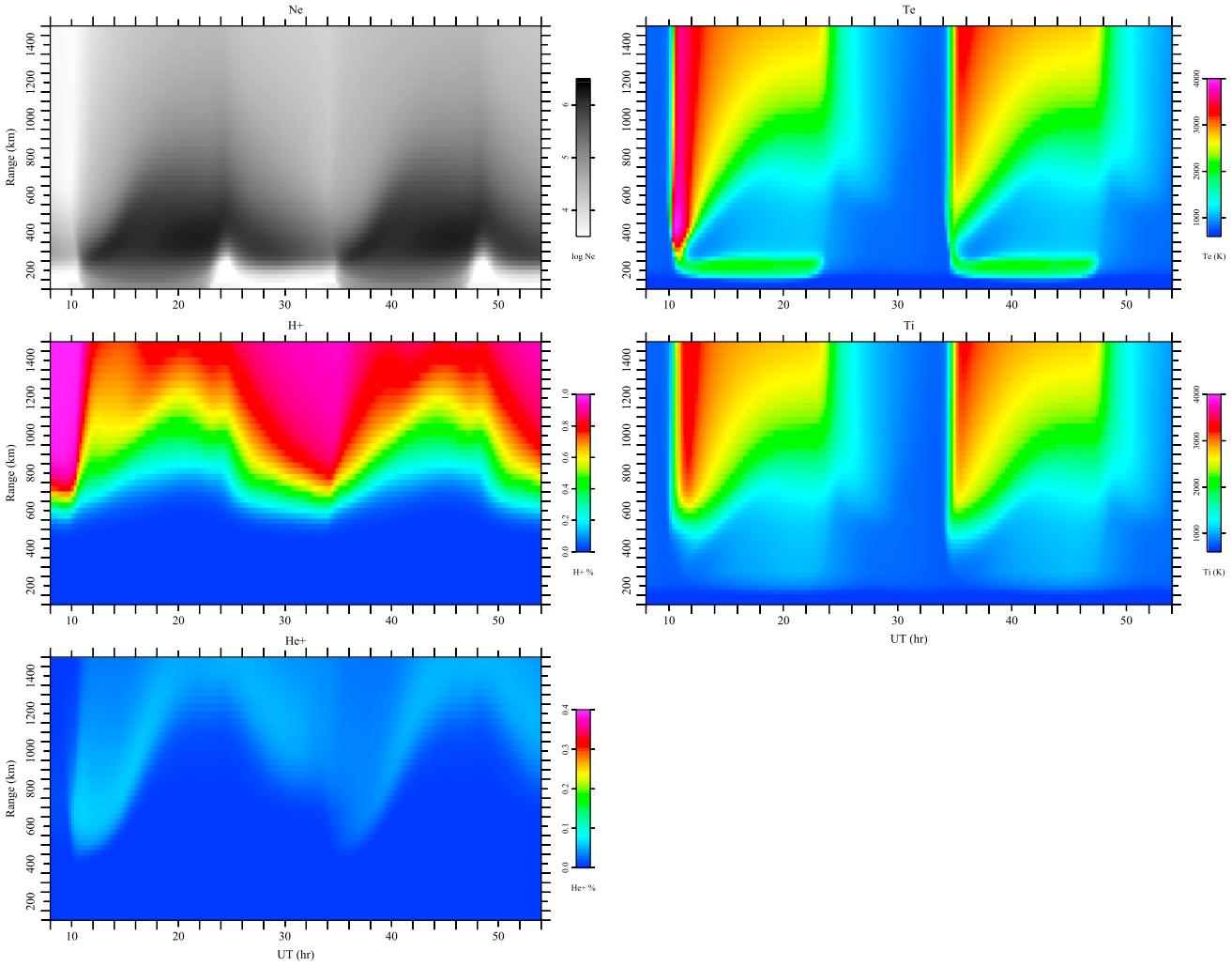

Figure 6. SAMI2-PE model simulations of the March 2013 Jicamarca incoherent scatter data plotted using the same format as Figure 3. UT = LT + 5 h.

SAMI2 splits parallel and perpendicular transport into successive operations. The latter operation is governed by magnetic dipole geometry and prescribed vertical $E \times B$ drifts. The thermodynamic effect of perpendicular convection due to $E \times B$ drifts is introduced by making electron and ion number density and temperature inversely proportional to the volume of the flux tube element the plasma inhabits. This implied adiabatic heating and cooling with 2 degrees of freedom. The effects of zonal transport are not considered in this 2-D model.

The SAMI2 model was augmented recently with an expanded treatment of energetic electron transport by *Varney et al.* [2012]. This model considers electron transport with multiple pitch angle streams and includes cascade and pitch angle scattering effects as well as provisions for secondary ionization and degradation through elastic and inelastic collisions.

Simulations were run for the conditions of the March and September 2013 experiments at Jicamarca, and the results are shown, respectively, in Figures 6 and 7. The simulations begin from "cold starts" and require approximately 24 h to reach dynamic equilibrium. We regard the latter portions of the simulations as being most meaningful. The model is not data driven here but yields results expected to be representative of the climatology. It is not expected to reproduce day-to-day variability.

Note that the simulation is able to predict different temperatures for different ions. The ion temperature plotted in this paper are for oxygen ions. Hydrogen ions are found to be up to about 5% warmer than oxygen ions at some altitudes briefly during the morning heating phase. This is a small difference which justifies fitting the ISR data for single-ion temperatures.

©2015. American Geophysical Union. All Rights Reserved.

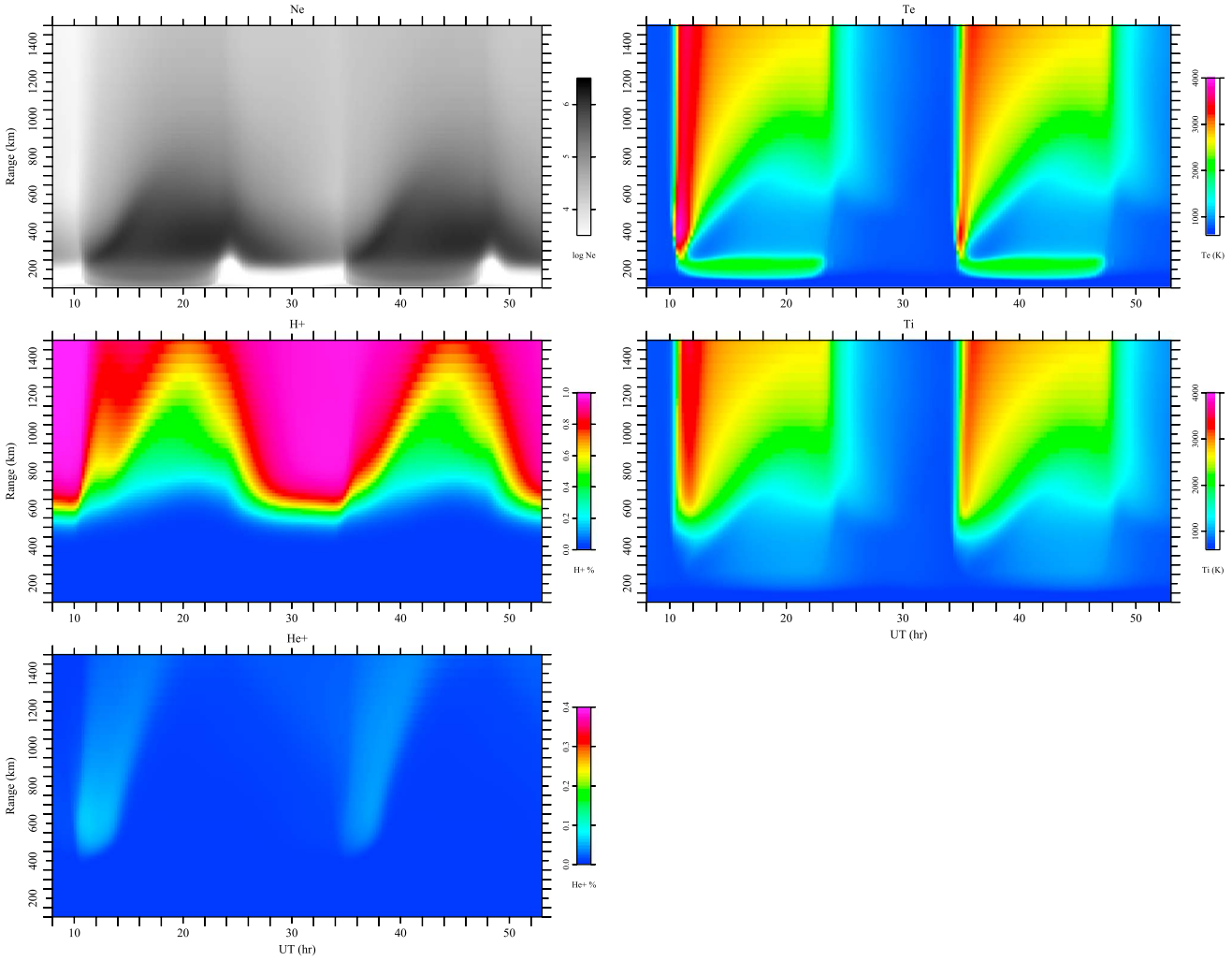

Figure 7. Same as Figure 6 only for September 2013 conditions. UT = *LT* + 5 h.

In many respects, the simulations capture the salient features of the Jicamarca data sets, including the gross diurnal variations in the electron and ion temperature, the plasma density, and the light-ion composition. Observed and simulated plasma number densities share very similar morphologies, in particular. The diurnal behavior of h_t in simulation is similar to what is observed although it is somewhat higher in simulation, varying between about 700–1100 km in the March runs and 600–1200 km in the September runs. Moreover, the oxygen ion fraction remains significant at the highest altitudes shown in simulation during the daytime whereas it is always a minor constituent at 1500 km altitude in the observations.

The morphology of the He^+ layers in the simulations is also similar to what is observed in the ISR measurements. Helium ion abundance is the greatest in the early morning in a layer that rises and falls with h_t. Helium ion densities are greater in the March run than in the September run. The simulated He^+ densities are somewhat greater than what is observed, particularly in the March run which also places the layer at somewhat higher altitudes. These discrepancies are consistent since the charge exchange reactions that remove helium ions run more slowly at higher altitudes.

The simulated electron and ion temperatures are similar to radar observations in the bottomside but differ markedly in the topside. The simulated temperatures are considerably lower than observations around sunrise and then significantly higher throughout much of the rest of the day. The midday temperature minimum in simulation is relatively modest compared to what is observed and is confined to altitudes below about 1300 km.

©2015. American Geophysical Union. All Rights Reserved.

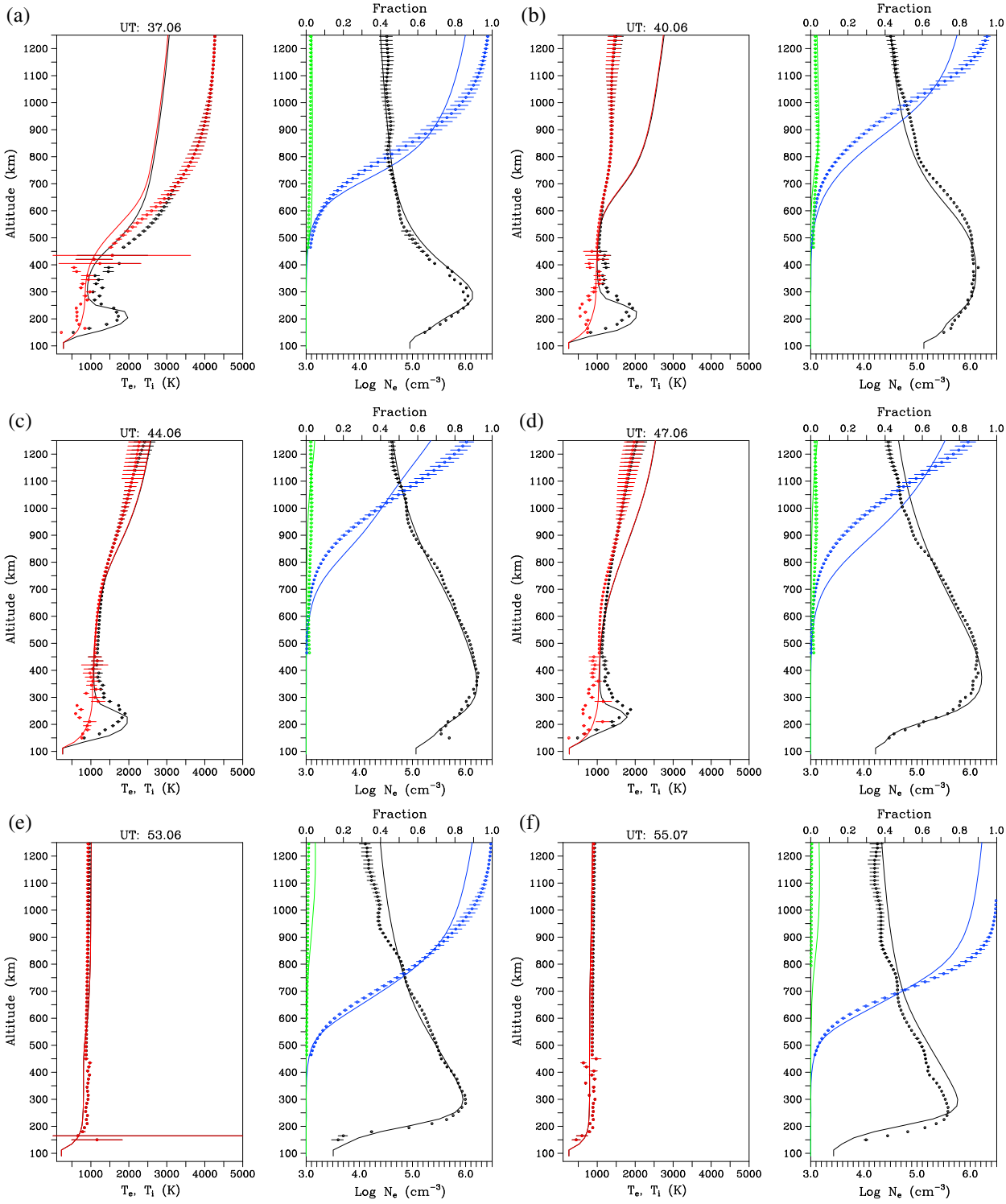

Figure 8. Measured and modeled profiles for six local times during the 12 March 2013 experiments. Experimental and model results are shown with and without error bars, respectively. In the leftmost panel in each case, red and black curves represent electron and ion temperatures, respectively. In the rightmost panels in each case, black, blue, and green curves represent electron density, H^+ fraction, and He^+ fraction profiles, respectively. UT = LT + 5 h.

A more detailed comparison between the Jicamarca and SAMI2-PE results is made in Figure 8 which shows measured and modeled state parameter profiles for six different local times extracted from 12 March 2013. The measured and simulated electron density profiles can be seen here to be remarkably similar, although there is a tendency for the simulation overestimate topside electron densities at night while

©2015. American Geophysical Union. All Rights Reserved.

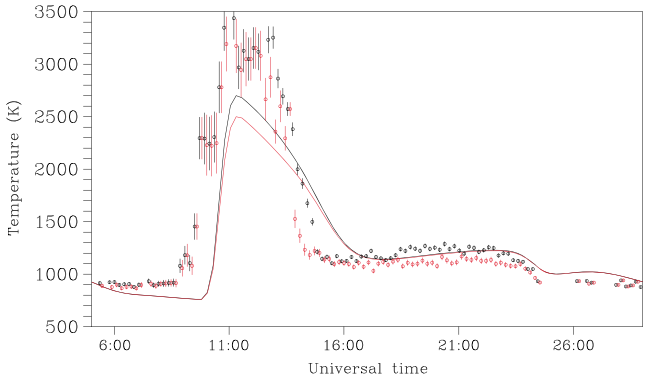

Figure 9. Comparisons of modeled (solid lines) and measured (plotted symbols) of electron (black) and ion (red) temperatures at an altitude of 600 km for the 12 March 2013 period. UT = LT + 5 h.

underestimating them around midday. The measured and simulated composition profiles exhibit similar trends generally. The simulations reproduce the measured transition height h_t closely most of the time but underestimate the hydrogen ion fraction at the highest altitudes.

The most significant discrepancy is in the electron and ion temperature profiles between sunrise and midday. Whereas the ISR measurements exhibit a drastic downward swing in topside temperatures (2000 K or more) in the early morning hours, the simulations predict more gradual variations. This is illustrated in Figure 9, which compares modeled and measured temperatures at 600 km altitude on 12 March 2013. The 600 km altitude was chosen because the effect is clear here. The figure also illustrates how measured ionospheric temperatures increased from their nighttime value an hour before local sunrise, a feature which was not captured in by the model and which can most likely be attributed to the effects of zonal transport. The measured electron temperatures are markedly greater than the ion temperatures in the afternoon. Finally, measured plasma temperatures are uniform throughout the night whereas the model predicts decreasing temperatures throughout the night.

Further insight into the thermodynamics of the topside can be gained by examining the most important components of the thermal forcing of the electrons. Figures 10a and 10b illustrate the electron heating rates at the magnetic equator for various mechanisms included in SAMI2-PE for the times and conditions depicted in Figures 9a and 9b, i.e., shortly after sunrise and around midday, respectively. Electron heating is via energetic electrons transported upward along magnetic field lines from the F_1 region where they are principally created. In the topside, this heating is balanced mainly by thermal conduction back down

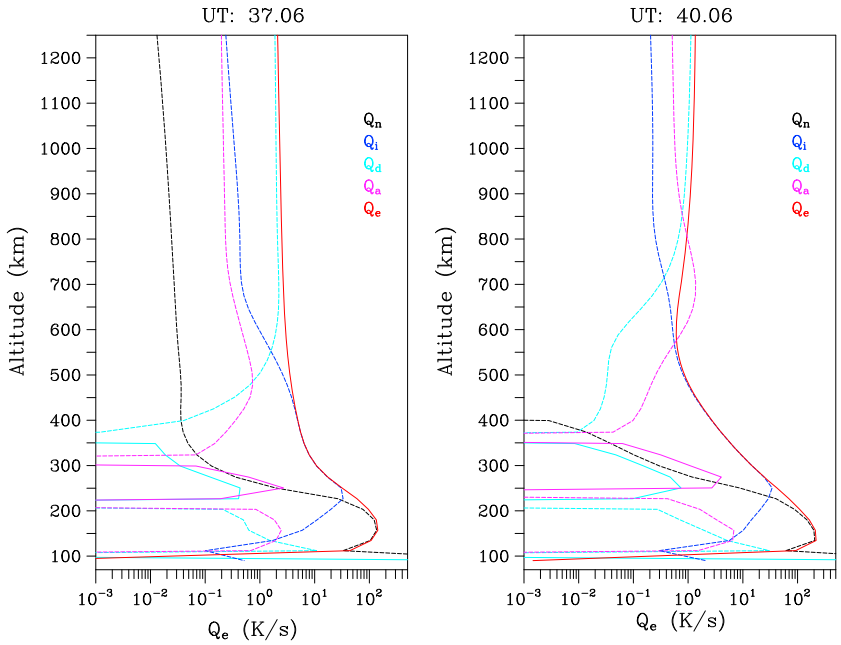

Figure 10. Electron heating rates calculated for the conditions and times shown in Figures 8a and 8b. Solid (dashed) lines imply heating (cooling) rates. Curves depict the effects of electron-neutral collisions (black), electron-ion collisions (blue), heat conduction (cyan), transverse convection (violet), and energetic electrons (red). UT = LT + 5 h.

©2015. American Geophysical Union. All Rights Reserved.

the field lines in the direction of the *F* peak. In Figure 10a, these two mechanisms nearly balance throughout most of the topside, with cooling through electron-ion collisions in the highly rarefied plasma only becoming significant below about 600 km.

Heating by energetic electrons causes a substantial increase in plasma temperature in the topside at dawn when the plasma is rarefied and the heat capacity is low. Temperatures subsequently decrease as topside plasma density and heat capacity increases. Furthermore, with increasing topside plasma density and decreased electron mean free paths, energetic electron transport to the magnetic equator becomes somewhat less efficient. Electron heating in the topside is balanced by thermal conduction, ion cooling (to a greater extent than was the case earlier), and significantly by transverse convection. The last mechanism is associated with $E \times B$ drifts and the daily rapid ascent of the equatorial ionosphere. In simulation, this mechanism is the main agent for electron temperature reduction near the base of the topside for a few hours after sunrise.

More precisely, the plasma temperature in Figure 9 reflects the behavior of the equatorial ionization anomaly (EIA) which fills during the day as plasma is transported poleward under the action of the fountain effect and empties in the evening as the fountain effect reverses, partially refilling the equatorial ionosphere. The temperature peak between 1000 and 1300 UT (0500 and 0800 LT) corresponds to a time when the $E \times B$ drift is weak and the EIA is undeveloped. Increased $E \times B$ drifts between 1300 and 1600 UT (0800 and 1100 LT) result in increased electron density and decreased temperature at the equator. The EIA subsequently becomes more developed between 1600 and 2100 UT (1100 and 1700 LT) as plasma is transported away from the equator, and the temperature increases somewhat as a result. Finally, the reverse fountain refills the equatorial ionosphere somewhat between about 2300 and 2400 UT (1800 and 1900 LT), and the plasma temperature drops once again.

The meridional winds, meanwhile, are essentially convergent at night and divergent during the day, leading to enhanced *F* layer densities in the former case and reduced in the latter. The diurnal pattern of the meridional winds, therefore, counters the diurnal pattern of the $E \times B$ convection, helping to regulate topside temperatures in large part. We find that the model results can be brought into somewhat better agreement with the data presented here by (a) scaling the $E \times B$ drifts from the *Scherliess and Fejer* [1999] model by a factor greater than 1 or (b) by scaling the meridional winds from HWM93 by a factor less than 1. This is not to suggest that these models are not representative of reality. Rather, we merely highlight the sensitivity of the model results to forcing which went unmeasured in these cases.

Improving congruity between the model and the data may require augmentation of the transport phenomena included in the model. *Blelly and Schunk* [1993] compared transport in models based on Maxwellian distribution functions including 5-, 8-, and 13-moment models along with a 16-moment equation set based on bi-Maxwellian distributions. They found important differences between the "standard" five-moment treatment and the other treatments at the altitudes of interest here. The eight-moment equations arise from assuming functional dependencies of the distribution functions on heat flow. This leads to corrections to the momentum equations pertaining to interspecies heat flow differences (thermal diffusion effects) and to the energy equations pertaining to interspecies velocity differences (diffusive thermal and thermoelectric effects.) The corrections may be important in the context not only of the polar wind for which they were considered but also in the equatorial topside.

For example, diffusive thermal and thermal diffusion effects imply that the electron thermal conductivity should involve both electron-electron and electron-ion Coulomb collisions, whereas only the former enter into the heat flow equations used in the five-moment standard set [*Blelly and Schunk*, 1993]. The thermal conductivity decreases when these effects are considered, meaning that the equilibrium electron temperatures in the topside should increase. The thermoelectric effect becomes another potential heat source for electrons when the return current associated with the energetic electrons is considered. Finally, thermal diffusion leads to upward transport of heavy ions predominantly and to an overall increase in topside plasma density [*Blelly and Schunk*, 1993]. As discussed above, this would have the effect of lowering temperatures in the topside.

Another issue is the neglect of the ambipolar field in the treatment of energetic electron transport. The ambipolar field undergoes a regular diurnal variation that should modulate the ability of suprathermal

©2015. American Geophysical Union. All Rights Reserved.

electrons to penetrate to the topside. A prescription for including the effect was provided by the polar wind analysis conducted recently by *Varney et al.* [2014] and references therein.

5. Summary and Conclusion

The full-profile incoherent scatter analysis used at Jicamarca has been updated and is now used routinely for topside data analysis. The analysis has been simplified and streamlined and can now run in real time on a single I7 processor core under nominal experimental circumstances. Experiments performed in March and September of 2013 during low solar flux conditions yielded state parameter profiles to altitudes of about 1500 km with a cadence of about 10 min. Results were consistent from day to day and between March and September, allowing for the fact that the solar flux index was somewhat higher in March (125) than in September (95).

The main features of the data sets include a regular, sawtooth-like diurnal variation in the h_t transition height, the appearance of weak helium ion layers just below h_t, and drastic elevations in electron and ion temperatures at sunrise followed by distinct depressions around local noon. This is the first unambiguous measurement of He^+ layers at Jicamarca in many years and the first time density, temperature, and light-ion composition have been measured self-consistently.

The SAMI2-PE model recovers the most salient features of the radar data set. The most significant discrepancy is the topside electron and ion temperatures which do not exhibit the kind of extremes in simulation found in the observations. Since we have neither $E \times B$ drift nor neutral wind measurements to accompany the model analysis, both drivers are modeled empirically, a factor which may be contributing to the discrepancy. SAMI2-PE also neglects some potentially important terms in its treatment of electron thermodynamics—parallel advection and diffusive thermal and thermoelectric effects in particular. The significance of these and other neglected phenomena in the equatorial topside remains to be assessed.

It is important to recognize that the plasma temperature in the topside over Jicamarca is controlled by energetic electron production at off-equatorial locations, in the midlatitude ionization anomalies notably. Future modeling studies of this kind will need to incorporate regional in addition to local observations. Networks of ionosondes, HF beacons, and GPS receivers have been deployed to Jicamarca's longitude sector in recent years. It should be possible to correlate state parameters in the topside with anomaly development and, perhaps ultimately, to diagnose the condition of the ionosphere regionally on the basis of local profile measurements.

Acknowledgments

The Jicamarca Radio Observatory is a facility of the Instituto Geofisíco del Perú operated with support from NSF award AGS-1433968 through Cornell. The help of the staff is much appreciated. Research of J.D.H. was supported by NRL Base Funds. Data used for this publication are available through the Madrigal database (http://www.openmadrigal.org). We thank the CINDI team for making data available for this study. CINDI data are available at http://cindispace.utdallas.edu/data.html.

Michael Liemohn thanks Ildiko Horvath and another reviewer for their assistance in evaluating the paper.

References

Aponte, N., C. G. M. Brum, M. P. Sulzer, and S. A. Gonzalez (2013), Measurements of the O^+ to H^+ transition height and ion temperatures in the lower topside ionosphere over Arecibo for equinox conditions during the 2008–2009 extreme solar minimum, *J. Geophys. Res. Space Physics*, *118*, 4465–4470, doi:10.1002/jgra.50416.

Aster, R. C., B. Borchers, and C. H. Thurber (2005), *Parameter Estimation and Inverse Problems*, Elsevier, New York.

Bailey, G. J. (1983), The effect of a meridional $\mathbf{E} \times \mathbf{B}$ drift on the thermal plasma at L = 1.4, *Planet. Space Sci.*, *31*, 389–409.

Bailey, G. J., and R. A. Heelis (2000), Ion temperature troughs induced by a meridional neutral air wind in the night-time equatorial topside ionosphere, *Planet. Space Sci.*, *28*, 895–906.

Bailey, G. J., R. Sellek, and Y. Rippeth (1993), A modelling study of the equatorial topside ionosphere, *Ann. Geophys.*, *11*, 263–272.

Balan, N., K. I. Oyama, G. J. Bailey, S. Fukao, S. Watanabe, and M. A. Abdu (1997), A plasma temperature anomaly in the equatorial topside ionosphere, *J. Geophys. Res.*, *102*, 7485–7492.

Banks, P. M., R. W. Schunk, and W. J. Raitt (1976), The topside ionosphere: A region of dynamic transition, *Annu. Rev. Earth Planet. Sci.*, *4*, 381–440.

Blelly, P. L., and R. W. Schunk (1993), A comparative study of the time-dependent standard 8-, 13-, and 16-moment transport formulations iof the polar wind, *Ann. Geophys.*, *11*, 443–469.

Bowles, K. L., G. R. Ochs, and J. L. Green (1962), On the absolute intensity of incoherent scatter echoes from the ionosphere, *J. Res. Nat. Bur. Stand. D. Radio Propag.*, *66D*, 395–340.

De-Boor, C. (1978), *A Practical Guide to Splines*, Springer, New York.

Farley, D. T. (1969a), Faraday rotation measurements using incoherent scatter, *Radio Sci.*, *4*, 143–152.

Farley, D. T. (1969b), Incoherent scatter correlation function measurements, *Radio Sci.*, *4*, 935–953.

González, S. A., and M. P. Sulzer (1996), Detection of He^+ layering in the topside ionosphere over Arecibo during equinox solar minimum conditions, *Geophys. Res. Lett.*, *23*, 2509–2512.

González, S. A., B. G. Fejer, R. A. Heelis, and W. B. Hanson (1992), Ion composition of the topside equatorial ionosphere during solar minimum, *J. Geophys. Res.*, *97*, 4299–4303.

González, S. A., M. P. Sulzer, M. J. Nicolls, and R. B. Kerr (2004), Solar cycle variability of nighttime topside helium ion concentration over Arecibo, *J. Geophys. Res.*, *109*, A07302, doi:10.1029/2003JA010100.

Heelis, R. A., and W. B. Hanson (1998), Measurements of thermal ion drift velocity and temperature using planar sensors, in *Measurement Techniques in Space Plasmas: Particles, Geophys. Monogr. Ser.*, vol. 102, edited by R. F. Pfaff, J. E. Borovsky, and D. T. Young, pp. 61–71, AGU, Washington, D. C.

©2015. American Geophysical Union. All Rights Reserved.

Heelis, R. A., W. B. Hanson, and G. J. Bailey (1990), Distributions of He^+ at middle and equatorial latitudes during solar maximum, *J. Geophys. Res.*, *95*, 10,313–10,320.
Heelis, R. A., W. R. Coley, A. G. Burrell, M. R. Hairston, G. D. Earle, M. D. Perdue, R. A. Power, L. L. Harmon, B. J. Holt, and C. R. Lippincott (2009), Behavior of the O^+/H^+ transition height during the extreme solar minimum of 2008, *Geophys. Res. Lett.*, *36*, L00C03, doi:10.1029/2009GL038652.
Holt, J. M., D. A. Rhoda, D. Tetenbaum, and A. P. van Eyken (1992), Optimal analysis of incoherent scatter radar data, *Radio Sci.*, *27*, 435–447.
Huba, J. D., G. Joyce, and J. A. Fedder (2000), Sami2 is another model of the ionosphere (SAMI2): A new low-latitude ionospheric model, *J. Geophys. Res.*, *105*, 23,035–23,054.
Huuskonen, A., and M. S. Lehtinen (1996), The accuracy of incoherent scatter measurements: Error estimates valid for high signal levels, *J. Atmos. Terr. Phys.*, *58*, 453–463.
Hysell, D. L., F. S. Rodrigues, J. L. Chau, and J. D. Huba (2008), Full profile incoherent scatter analysis at Jicamarca, *Ann. Geophys.*, *26*, 59–75.
Hysell, D. L., J. L. Chau, and J. D. Huba (2009), Topside measurements at Jicamarca during solar minimum, *Ann. Geophys.*, *27*, 427–439.
Kudeki, E., and M. Milla (2011), Incoherent scatter spectral theories part I: A general framework and results for small magnetic aspect angles, *IEEE Trans. Geosci. Remote Sens.*, *49*(1), 315–328.
Lawson, C. W., and R. J. Hanson (1987), *Solving Least Squares Problems*, SIAM, Philadelphia, Pa.
Lehtinen, M. S. (1986), Statistical theory of incoherent scatter radar measurements, *Tech. Rep. 86/45*, Eur. Incoherent Scatter Sci. Assoc., Kiruna, Sweden.
Lehtinen, M. S., and A. Huuskonen (1996), General incoherent scatter analysis and GUISDAP, *J. Atmos. Terr. Phys.*, *58*, 435–452.
Levenberg, K. (1944), A method for the solution of certain non-linear problems in least squares, *Q. Appl. Math.*, *2*, 164–168.
Marquardt, D. (1963), An algorithm for least-squares estimation of nonlinear parameters, *SIAM J. Appl. Math.*, *11*, 431–441.
Menke, W. (1984), *Geophysical Data Analysis: Discrete Inverse Theory*, Academic, New York.
Milla, M., and E. Kudeki (2006), F-region electron density and Te/Ti measurements using incoherent scatter power data collected at ALTAIR, *Ann. Geophys.*, *24*, 1333–1343.
Milla, M., and E. Kudeki (2011), Incoherent scatter spectral theories part II: Modeling the spectrom for modes propagating perpendicular to B, *IEEE Trans. Geosci. Remote Sens.*, *49*(1), 329–345.
Nygrén, T. (1996), *Introduction to Incoherent Scatter Measurements*, Invers Oy, Sodankylä, Finland.
Pingree, J. E. (1990), Incoherent scatter measurements and inferred energy fluxes in the equarotial F-region ionosphere, PhD thesis, Cornell Univ., Ithaca, New York.
Rishbeth, H., T. E. van Zandt, and W. B. Hanson (1977), Ion temperature troughs in the equatorial topside ionosphere, *Planet. Space Sci.*, *25*, 629–642.
Scherliess, L., and B. G. Fejer (1999), Radar and satellite global equatorial *F*-region vertical drift model, *J. Geophys. Res.*, *104*, 6829–6842.
Schunk, R. W., and A. F. Nagy (2004), *Ionospheres: Physics, Plasma Physics, and Chemistry*, Cambridge Univ. Press, Cambridge, U. K.
Sulzer, M. P., and S. Gonzalez (1999), The effect of electron Coulomb collisions on the incoherent scatter spectrum in the F region at Jicamarca, *J. Geophys. Res.*, *104*, 22,535–22,552.
Sulzer, M. P., and S. A. González (1996), Simultaneous measurements of O^+ and H^+ temperatures in the topside ionosphere over Arecibo, *Geophys. Res. Lett.*, *23*, 3235–3238.
Tarantola, A. (1987), *Inverse Theory*, Elsevier, New York.
Varney, R. H., D. Hysell, and J. D. Huba (2011), Sensitivity studies of equatorial topside electron and ion temperatures, *J. Geophys. Res.*, *116*, A06321, doi:10.1029/2011JA016549.
Varney, R. H., W. Swartz, D. Hysell, and J. Huba (2012), SAMI2-PE: A model of the ionosphere including multi-stream interhemispheric photoelectron transport, *J. Geophys. Res.*, *117*, A06322, doi:10.1029/2011JA017280.
Varney, R. H., D. Hysell, and J. Huba (2013), Sources of variability in equatorial topside ionospheric and plasmaspheric temperatures, *J. Atmos. Sol. Terr. Phys.*, *103*, 83–93, doi:10.1016/j.jastp.2012.12.024.
Varney, R. H., S. C. Solomon, and M. J. Nicolls (2014), Heating of the sunlit polar cap ionosphere by reflected photoelectrons, *J. Geophys. Res. Space Physics*, *119*, 8660–8684, doi:10.1002/2013JA019378.
Venkatraman, S., and R. Heelis (1999), Longitudinal and seasonal variations in nighttime plasma temperatures in the equatorial topside ionosphere during solar maximum, *J. Geophys. Res.*, *104*, 2603–2611.
Venkatraman, S., and R. Heelis (2000), Interhemispheric plasma flows in the equatorial topside ionosphere, *J. Geophys. Res.*, *105*, 18,457–18,464.
West, K. H. (2009), Observations of He^+ concentrations in the topside ionosphere under equinox conditions near solar minimum: Morningside morphology, *J. Geophys. Res.*, *114*, A09307, doi:10.1029/2008JA014014.
Woodman, R. F. (1991), A general statistical instrument theory of atmospheric and ionospheric radars, *J. Geophys. Res.*, *96*, 7911–7915.
Woodman, R. F. (2004), On a proper electron collision frequency for a Fokker-Planck collision model with Jicamarca applications, *J. Atmos. Sol. Terr. Phys.*, *66.17*, 1521–1541.

©2015. American Geophysical Union. All Rights Reserved.